Springer

KSME

Journal of Mechanical Science and Technology 32 (12) (2018) 5927~5936
www.springerlink.com/content/1738-494x(Print)/1976-3824(Online)
DOI 10.1007/s12206-018-1144-2

Numerical study on the two-phase flow pattern and temperature distribution in a loop thermosyphon as a defrost device at the evaporator in the refrigerator †

Seong Hyun Park[1], Young Soo Kim[2], Seung Youn Kim[2], Yong Gap Park[3,*] and Man Yeong Ha[1,*]

[1]*School of Mechanical Engineering, Pusan National University, San 30, Jangjeon-dong, Geumjeong-gu, Busan 609-735, Korea*
[2]*Home Appliance and Air Solution Company, LG Electronics, Gaeumjeong-Dong, Seong San Gu, Changwon, Korea*
[3]*Rolls-Royce and Pusan National University Technology Centre in Thermal Management, Jang Jeon 2-Dong, Geum Jeong Gu, Busan 609-735, Korea*

(Manuscript Received March 26, 2018; Revised August 8, 2018; Accepted September 21, 2018)

Abstract

This paper discusses the two-phase flow pattern and temperature distribution in a loop thermosyphon as a defrost device at the surface of the evaporator in the refrigerator with different heater locations and different heating power. A computational fluid dynamics (CFD) study was carried out using ANSYS FLUENT 15.0. The volume of fluid (VOF) model was considered to simulate evaporation and condensation at the heater surface using user-defined functions (UDFs). 2D geometries were developed with a heater inserted in the loop thermosyphon. The simulation results were verified using Fadhl's experimental and numerical temperature data [2]. The maximum difference is 2.4 % between the calculated data and Fadhl's data. The two-phase flow pattern and the temperature field varied with the different heater locations and heating power values. The thermal performance was evaluated based on the average temperature and temperature uniformity inside the loop thermosyphon.

Keywords: Loop thermosyphon; Location of a heater; Heating power; Evaporation and condensation; Temperature uniformity inside the loop thermosyphon; Average temperature inside the loop thermosyphon

1. Introduction

A two-phase loop thermosyphon has been widely used in a vast range of engineering applications, such as an electrical cooling system, solar energy system [1]. A loop thermosyphon has evaporation section and condensation section, similar to other thermosyphon. Heat from a heater enters the evaporation section, and the working fluid absorbs an amount of heat proportional to the latent heat of evaporation, which is sufficient to change the fluid from liquid to vapor [2]. The vapor then flows to the condensation section, where the heat is transferred from the vapor to the liquid. In the condensation section, the vapor condenses and returns as a liquid to the evaporation section due to the occurrence of pressure difference induced by the nucleation of vapor bubbles in the evaporation section.

Many numerical studies have focused on the development of mathematical models by calculating the thermal resistance of the system or using 1D thermal network analysis [3-7]. However, it is impossible to identify a bubble generation mechanism and to visualize the temperature distribution and two-phase flow pattern with these methodologies. Therefore, computational fluid dynamics (CFD) simulation is needed to understand the heat and mass transfer mechanism in the heat pipe. However, CFD studies of multiphase flow with phase changes are very computationally expensive compared to single-phase problems. With rapid advances in parallel computing technologies, many CFD studies on heat pipes are now being reported [1, 2, 8-20].

Various studies have investigated multiphase flow simulations for thermosyphons [1, 2, 9-15]. De Schepper et al. [14] proposed equations for the mass and momentum source to model evaporation and condensation in a thermosyphon. Numerical temperature data were validated with experimentally measured temperatures. Alizadehdakhel et al. [15] modeled a gas and liquid two-phase flow along with the simultaneous evaporation and condensation phenomena in a thermosyphon. The volume of fluid (VOF) technique was used to model the interaction between these phases. They concluded that CFD is a useful tool for modeling and explaining the complex two-phase flow and heat transfer in a thermosyphon.

Fadhl et al. [1, 2] built a CFD model to simulate the two-phase flow and heat transfer phenomena of a thermosyphon. The mass and energy source terms proposed by De Schepper et al. [14] were applied to model the evaporation and condensation process. They conducted CFD calculations using different heating power input in the evaporation section. The pre-

*Corresponding author. Tel.: +82 51 510 3395, 82 51 510 2440, Fax.: +82 51 515 3101, 82 515 3101
E-mail address: pyg777@pusan.ac.kr, myha@pusan.ac.kr
† Recommended by Associate Editor Chang Yong Park

dicted temperature profiles from the CFD calculations and the experimental temperature data showed good agreement.

Lin et al. [16] simulated the two-phase flow behavior in a pulsating heat pipe. The continuum surface force (CSF) model was used to consider the effect of surface tension. Mass and energy source terms were also modeled to simulate the evaporation and condensation phenomena. Micro oscillating heat pipes were simulated with different heat transfer lengths and inner diameters at different heating powers, and the results were compared with experimental results under the same conditions.

Pouryoussefi et al. [17] numerically investigated the chaotic flow in a two-dimensional closed-loop pulsating heat pipe. They analyzed the chaotic flow in a pulsating heat pipe under several conditions. The chaos in the pulsating heat pipe was investigated using time series analysis of the adiabatic wall temperature, correlation dimension, power spectrum density, Lyapunov exponent, and autocorrelation function. Chaotic behavior was observed under several operating conditions.

The density was considered as a constant value in these papers. However, the pressure is increased when a large amount of heat is applied to the evaporation section. Therefore, the density of the vapor would increase over time. A limited number of papers considered the increase of vapor density in their calculations [18, 19].

Kalata et al. [18] carried out a numerical simulation of the performance of pressure swirl atomizers. The mass transferred model was based on the fluid properties and the characteristic diameter of the nozzle. The variation of the vapor density was modeled based on the incompressible ideal gas law based on the operating pressure. Lei et al. [19] suggested a CFD model to investigate the thermal performance and pressurization behaviors for a pressurized discharge process. A multi-component ullage including helium and propellant vapor with evaporation and condensation processes was considered. The ideal gas law was used to calculate the ullage density.

In a recent study, a loop thermosyphon was utilized in the refrigerator to melt frost layer at the surface of evaporator in the refrigerator [20]. Gu et al. developed bubble jet loop heat pipe (BJLHP), which is similar to conventional loop thermosyphon but has a cartridge heater inside a thermosyphon to enhance nucleate boiling at the surface of heater. They conducted experiments in a refrigerator using a loop thermosyphon with varying power consumption and filling ratio and compared temperature between electrical heater and loop thermosyphon. They concluded that it could be possible to increase heat capacity, decrease electric power consumption and minimize maximum average temperature by applying BJLHP to evaporator instead of electric heater.

However, they didn't visualize temperature distribution and bubble circulation features inside a loop thermosyphon. The BJLHP is different from other conventional heat pipe or thermosyphon in that the heater is located inside a BJLHP, while heater is located outside wall of evaporation region in other heat pipes. The bubble generation mechanism and two-phase flow pattern and temperature distribution inside BJLHP are different from those in other heat pipes. Therefore, in the present study, CFD study on the loop thermosyphon as a defrost device was conducted to analyze detailed bubble detachment mechanism at the heater surface and visualize two-phase flow pattern and temperature distribution inside a loop thermosyphon with different the location of a heater. The thermal performance was evaluated based on the average temperature and temperature uniformity inside the loop thermosyphon.

2. Numerical methodology

The motion of bubbles and the temperature field in the loop thermosyphon were described using equations for the mass continuity, momentum, energy, turbulent, and volume fraction. The VOF method was applied to describe the interface between the vapor and liquid. In this method, the velocity and temperature fields were shared among the phases. The volume fraction equation, momentum equation, energy equation, and turbulent equations were solved throughout the computational domain. The properties appearing in the transport equations are determined by the presence of the component phases in each control volume. The volume fraction of each fluid in each computational cell is tracked throughout the domain by defining a volume fraction conservation equation [21]. A *k-ω* model was used for the turbulent flow. The governing equations are the following:

Volume fraction equation

$$\frac{\partial(\alpha_v\rho_v)}{\partial t}+\nabla\cdot\left(\alpha_v\rho_v\vec{v}\right)=S_M. \tag{1}$$

Continuity equation

$$\frac{\partial\rho}{\partial t}+\nabla\cdot\left(\rho\vec{v}\right)=0. \tag{2}$$

Momentum equation

$$\frac{\partial}{\partial t}(\rho\vec{v})+\nabla\cdot(\rho\vec{v}\vec{v})=-\nabla p+\nabla\cdot\left[\mu\left(\nabla\vec{v}+\nabla\vec{v}^T\right)\right]+\rho\vec{g}+\vec{F}. \tag{3}$$

Energy equation

$$\frac{\partial}{\partial t}(\rho E)+\nabla\cdot\left(\vec{v}(\rho E+p)\right)=\nabla\cdot\left(k_{eff}\nabla T\right)+S_E \tag{4}$$

$$E=h-\frac{p}{\rho}+\frac{v^2}{2}. \tag{5}$$

Standard *k-ω* equations

$$\frac{\partial}{\partial t}(\rho k)+\nabla\cdot(\rho k\vec{v})=\nabla\cdot\left(\Gamma_k(\nabla k)\right)+G_k-Y_k \tag{6}$$

$$\frac{\partial}{\partial t}(\rho\omega)+\nabla\cdot(\rho\omega\vec{v})=\nabla\cdot\left(\Gamma_\omega(\nabla k)\right)+G_\omega-Y_\omega \tag{7}$$

where subscripts *l* and *v* indicate a liquid and vapor respec-

tively, ρ is the density, $\vec{v}$ is the velocity vector, μ is the viscosity, S_M is mass source term, E is the energy, p is the pressure, h is the enthalpy, S_E is the energy source term, G_k is the generation of turbulence kinetic energy due to the mean velocity gradient, G_ω is the generation of ω, Γ_k is the effective diffusivity of k and Γ_ω is the effective diffusivity of ω. The density and viscosity were defined as the volume-fraction-averaged values:

$$\rho = \alpha_v \rho_v + \alpha_l \rho_l \tag{8}$$

$$\mu = \alpha_v \mu_v + \alpha_l \mu_l \,. \tag{9}$$

The commercial code ANSYS FLUENT 15.0 and user-defined functions (UDFs) were used to specify customized source terms proposed by De Schepper et al. [14] to simulate the mass source and energy source for the evaporation and condensation processes. The mass source $S_{M,l}$ and $S_{M,v}$ are defined as follows:

Mass source term during the evaporation process:

$$S_{M,l} = -0.1 \rho_l \alpha_l \frac{T - T_{sat}}{T_{sat}} \tag{10}$$

$$S_{M,v} = -S_{M,l} \,. \tag{11}$$

Mass source term during the condensation process:

$$S_{M,l} = 0.1 \rho_v \alpha_v \frac{T_{sat} - T}{T_{sat}} \tag{12}$$

$$S_{M,v} = -S_{M,l} \tag{13}$$

where T and T_{sat} are the temperature of the mixture and the saturation temperature, respectively. Eq. (10) represents the amount of mass taken from the liquid phase during the evaporation process, and Eq. (11) represents the amount of mass added to the vapor phase during the evaporation process. Eq. (12) represents the amount of mass added to the liquid phase during the condensation process, and Eq. (13) represents the amount of mass taken from the vapor phase.

The energy source S_E is also defined to consider the latent heat of evaporation and the condensation process:

Energy source term during the condensation process:

$$S_E = -0.1 \rho_l \alpha_l L \frac{T - T_{sat}}{T_{sat}} \,. \tag{14}$$

Energy source term during the evaporation process:

$$S_E = 0.1 \rho_v \alpha_v L \frac{T_{sat} - T}{T_{sat}} \tag{15}$$

where L is the latent heat of evaporation.

Fig. 1 shows the CFD geometries developed to represent the loop thermosyphon. A heater is inserted inside the loop thermosyphon to generate bubbles. The diameter of BJLHP is

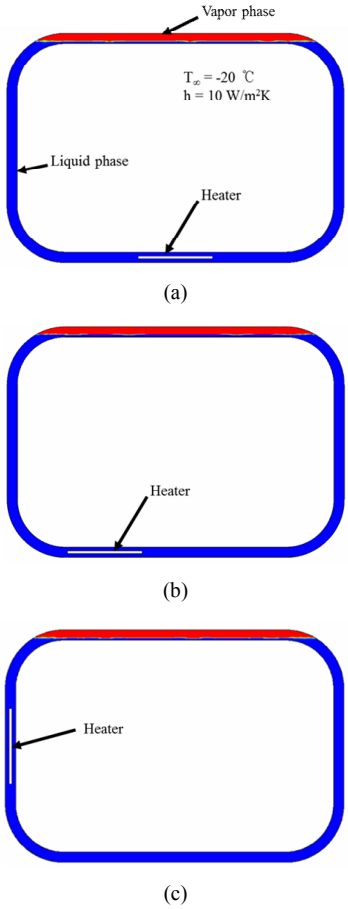

Fig. 1. Computational domain and boundary conditions for CFD simulation: (a) Cases 1 and 2 - A heater was located horizontally on the bottom center of loop thermosyphon; (b) cases 03 and 04 - a heater was located horizontally on the bottom left of loop thermosyphon; (c) cases 05 and 06 - a heater was located vertically on the left center of loop thermosyphon.

3.9 mm, the length of it is 128.2 mm and the height of it is 87.4 mm. To simulate the heat input, a constant heat flux is applied to the heater surface, which depends on the heating power input. Convective boundary conditions were applied at the outside walls to represent environmental conditions of loop thermosyphon inside a refrigerator. The heat transfer coefficient is 10 W / m^{2}K , and the free stream temperature is -20 °C at the outside walls.

Table 1 shows the test conditions considered in this study. The numerical study was conducted with different locations and heating power of the heater. Other conditions were the same in all cases, including the operating pressure, initial conditions, and filling ratio of R-134a. The filling ratio is the ratio of liquid to vapor ratio of R-134a, which is 0.8. The initial pressure and temperature of R-134a were set to 6 bar and -20 °C, respectively.

To compare of the effects of the heater location, three geometries with different heater locations were considered. In cases 01 and 02, the heater was located horizontally at the

Table 1. Tested conditions considered in this study.

	Heater location	Heating value
Case 01	Bottom center	$\dot{Q}_1$
Case 02	Bottom center	$2\dot{Q}_1$
Case 03	Bottom left	$\dot{Q}_1$
Case 04	Bottom left	$2\dot{Q}_1$
Case 05	Left center	$\dot{Q}_1$
Case 06	Left center	$2\dot{Q}_1$

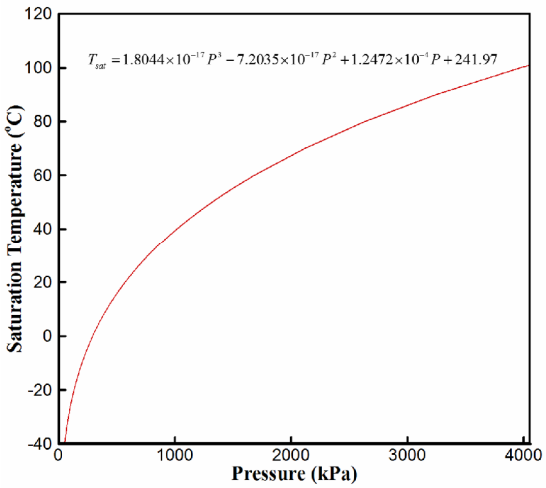

Fig. 2. Variation of saturation temperature with pressure.

bottom center of the loop thermosyphon. In cases 03 and 04, the heater was located horizontally on the bottom left of the loop thermosyphon. In cases 05 and 06, the heater was located vertically on the left center. To compare the effects, the heating power in cases 02, 04 and 06 was two times larger than that in cases 01, 03 and 05, respectively. Total six test cases were examined.

The working fluid inside the loop thermosyphon is R-134a. The ideal gas law is applied to consider the increase of density due to the increased pressure. Polynomial functions of temperature were used for other thermophysical properties such as the viscosity, thermal conductivity, specific heat, and liquid density. To create these functions, data were extracted from the NIST database [22]. All data were fitted with polynomial equations.

The saturation temperature varies with the pressure during the calculation. The evaporation mass transfer rate decreased as the saturation temperature increased. A plot of the saturation temperature with respect to pressure is shown in Fig. 2. The variation of the saturation temperature was considered as a polynomial function of pressure, which was created by fitting the data in Fig. 2. A detailed flow chart of the simulation is shown in Fig. 3.

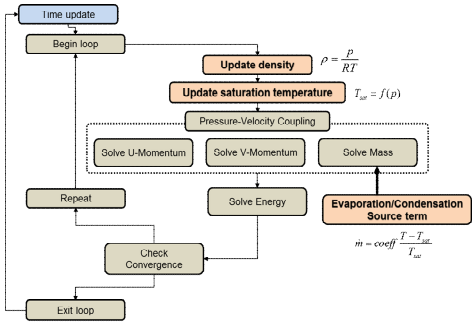

Fig. 3. Simulation flow chart.

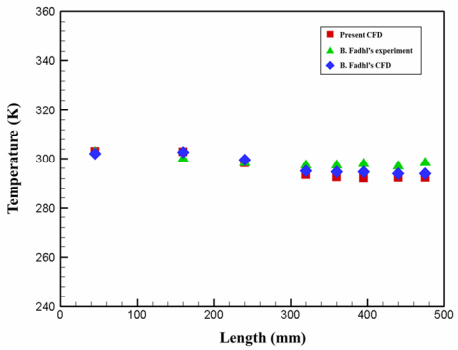

Fig. 4. Comparison of numerically calculated temperatures and Fadhl's calculated and experimentally measured temperature.

3. Results

3.1 Validation test

Because there is no information on the geometry of BJLHP and detailed boundary conditions and initial conditions for the experiments, the numerical simulation was validated using Fadhl's experimental and numerical temperature data [2], which is obtained from the experiment using circular type thermosyphon. They measured wall temperature of thermosyphon using eight thermocouples. The diameter of BJLHP is 3.9 mm, the length of it is 128.2 mm and the height of it is 87.4 mm. The surrounding temperature is 292.4 K and the value of heat added in the thermosyphon is 29.58 W. Fig. 4 qualitatively compares the calculated temperatures in the present study with Fadhl's results at the measured positions. The length in the figure means the length from bottom of thermosyphon. The distance between 0 mm to 200 mm indicates the evaporator section while the distance between 300 mm to 500 mm indicates condenser section. The middle section is adiabatic section.

The absolute percentage difference between CFD simulation and Fadhl's experimental results was calculated. The equations of absolute percentage difference are shown below:

$$Error_{EXP} = \frac{\left|T_{\exp,reference} - T_{CFD}\right|}{T_{CFD}} \times 100 \quad (16)$$

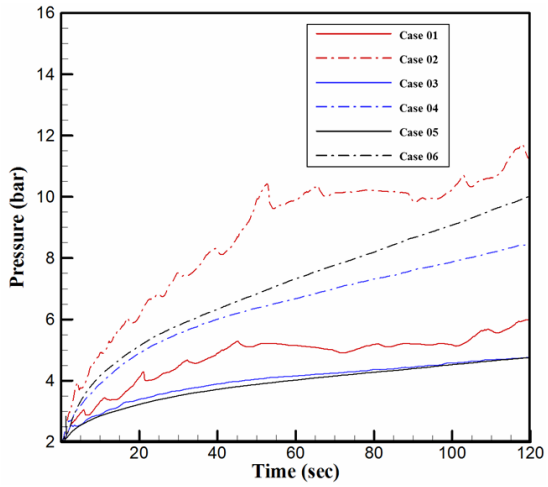

(a)

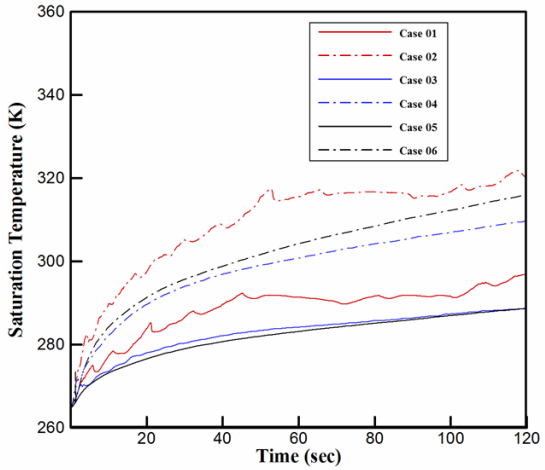

(b)

Fig. 5. Transient variation of (a) average pressure; (b) saturation temperature for each case.

$$Error_{CFD} = \frac{\left|T_{CFD,\text{reference}} - T_{CFD}\right|}{T_{CFD}} \times 100 \quad (17)$$

where $T_{\text{exp},reference}$ is the wall temperature which is measured experimentally by the Fadl et al., $T_{\text{CFD},reference}$ is the wall temperature which is calculated by Fadhl et al, and T_{CFD} is the wall temperature which is calculated in the present simulations. The absolute percentage difference between Fadhl's numerical results and our simulation results is below 0.8 %, while the absolute percentage difference between Fadhl's experimental data and our simulation results was about 2.4 %.

3.2 Variation of pressure and saturation temperature

Fig. 5 shows the transient variation of the average pressure and saturation temperature for each case. The temperature at the heater surface was increased by applying constant heat flux at the surface during calculations. The R-134a started to evaporate in the initial stages of the calculation when the temperature at the heater exceeded the saturation temperature. The temperature of heater surface increased and evaporation occurred continuously at the heater surface. Nucleated bubbles grew and detached over time. The average pressure increased due to the generation of bubbles at the heater surface, as shown in Fig. 5(a).

When the heater was located horizontally on the bot-tom left (cases 03 and 04) and vertically on the left center (cases 05 and 06) of the loop themosyphon, the average pressure curves increased gradually. However, when the heater was located horizontally on the bottom center (cases 01 and 02), the average pressure curves still increased but fluctuated over time, and the average pressure was higher than that in the other geometries because the bubbles repeatedly aggregated at the heater surface and detached from it. Fig. 5(b) shows the transient variation of the saturation temperature over time for each case. The saturation temperature varies with the pressure as shown in Fig. 2. Therefore, the tendency was similar to that of the average pressure in the loop thermosyphon. The evaporation mass transfer rate decreased over time because saturation temperature increased as pressure increased.

3.3 Mechanism of bubble detachment

Fig. 6 shows the volume fraction distribution around the heater in case 01 at different times. At the beginning of the heating process, the temperature around heater was increased by applying constant heat flux to the heater. Bubble nucleation occurred at the heater when the temperature at the heater surface exceeded the saturation temperature of R-134a. The nucleated bubbles grew over time and tended to move to the space between the top surface of the heater and the wall of the loop thermosyphon due to buoyancy. However, they did not detach until 5.8 s because of the surface tension at the wall. As a result, the bubbles aggregated at both the top and bottom surfaces of the heater between 1.2 and 5.8 s, as shown in Figs. 6(a)-(c).

The vapor layer grew continuously due to the nucleation of bubbles at the heater surface. The vapor layer was separated when its length exceeded the distance between the heater and the curved pipe of the loop thermosyphon. At 5.8 s, the vapor layer between the top surface of the heater and the curved part of the loop thermosyphon separated into large bubbles and a vapor layer because the buoyancy force was larger than the surface tension between the vapor layer and loop thermosyphon wall, as shown in Fig. 6(c).

The saturation temperature increased due to the increase of pressure over time. The temperature difference between the heater surface and saturated working fluid decreased because the saturation temperature increased. The evaporation mass transfer rate was proportional to the temperature difference between the heater surface and the saturated working fluid. Therefore, the evaporation mass transfer rate near the heater decreased over time, as shown in Figs. 6(d)-(f).

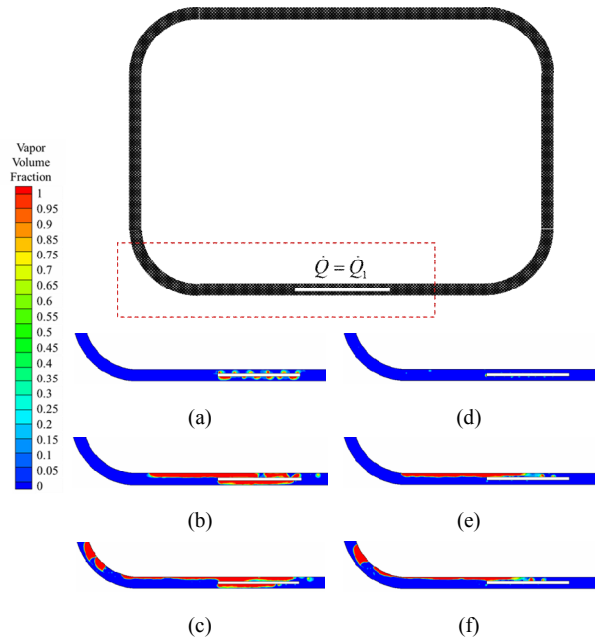

Fig. 6. Volume fraction distribution around a heater in case 01: (a) t = 1.2 s; (b) t = 4.8 s; (c) t = 5.8 s; (d) t = 33.7 s; (e) t = 45.0 s; (f) t = 45.3 s.

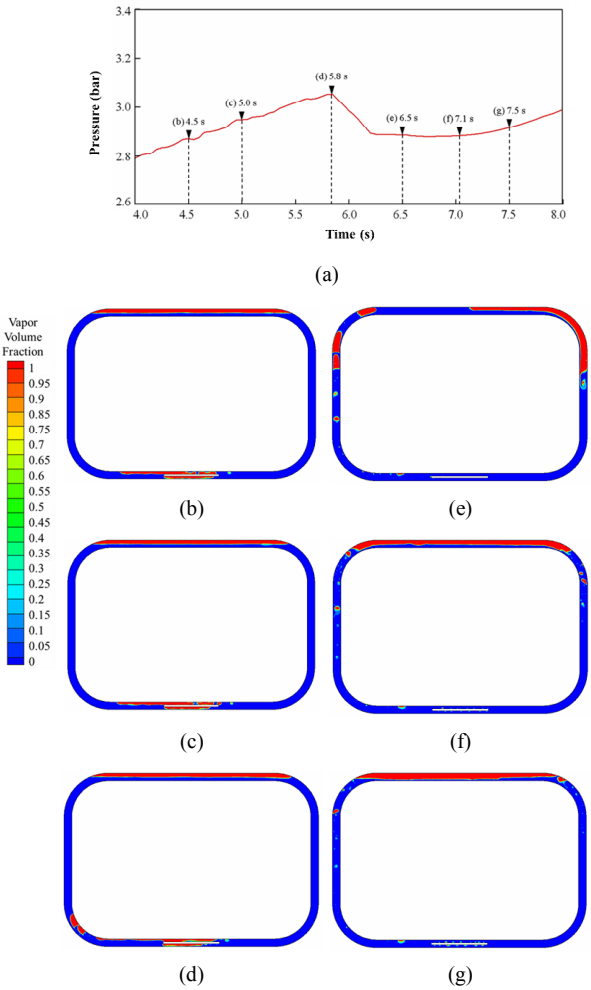

Fig. 7. (a) Variation of pressure between 4.0 s and 8.0 s and volume fraction distribution in case 01: (b) t = 4.5 s; (c) t = 5.0 s; (d) t = 5.8 s; (e) t = 6.5 s; (f) t = 7.1 s; (g) t = 7.5 s.

For detailed analysis of the bubble detachment mechanism, Fig. 7 shows the volume fraction distribution at the initial stage of operation in the whole thermosyphon and the variation of pressure at that time. The pressure increased until 5.8 s because the generated bubbles couldn't flow until the vapor layer was separated when its length exceeded the distance between the heater and the curved pipe of the loop thermosyphon as shown in Figs. 7(a)-(c). The large bubbles that separated from the vapor layer travelled upward and pushed the liquid and the top side of vapor layer in the clockwise direction between 5.8 s and 6.5 s, making a fluid flow in a clockwise direction as shown in Fig. 7(d). The top side of the vapor layer moved back to the left side of the loop thermosyphon between 6.5 s and 7.1 s because the momentum induced by the movement of detached bubbles decreased, as shown in Figs. 7(d)-(f), resulting in a rapid decrease of pressure as shown in Fig. 7(a). The pressure increased again when the vapor layer started to grow at the top heater surface.

Fig. 8 shows the volume fraction distribution around the heater in case 02 at different times. The heating power in case 02 was two times larger than that in case 01. The vapor layer grew quickly compared to case 01 due to the frequent nucleation of bubbles at the heater surface, as shown in Figs. 8(a) and (b). As a result, the time at which bubbles started to separate from the vapor layer in case 02 was shorter and the bubbles moved much faster compared to case 01, as shown in Fig. 8(c). The evaporation mass transfer rate decreased over time, similarly to case 01, as shown in Figs. 8(d)-(f).

Fig. 9 shows the volume fraction distribution around the heater in case 03 at different times. The distance between the heater and the curved pipe in case 03 was smaller than in case 01 because the heater was located horizontally on the bottom left of the loop thermosyphon. In the initial stage, bubbles nucleated due to the temperature difference between the heater and saturated working fluid. The generated bubbles tended to move upward due to the buoyancy force and aggregated at both the top and bottom surfaces of the heater, similarly to case 01. The bubble layer grew over time due to the nucleation of bubbles at the heater surface, as shown in Figs. 9(a) and (b). When the bubble layer reached the curved pipe, large bubbles separated from the vapor layer. The time at which bubbles started to separate from the vapor layer in case 03 was shorter than in case 01 because the distance between the left side of the heater and the curved pipe was much smaller than in case 01.

At 2.4 s, the large bubbles detached from the vapor layer, as shown in Fig. 9(c). The size of bubbles that detached from the heater decreased over time, as shown in Figs. 9(d)-(f), which is similar to cases 01 and 02. The mechanism of bubble detachment also changed over time.

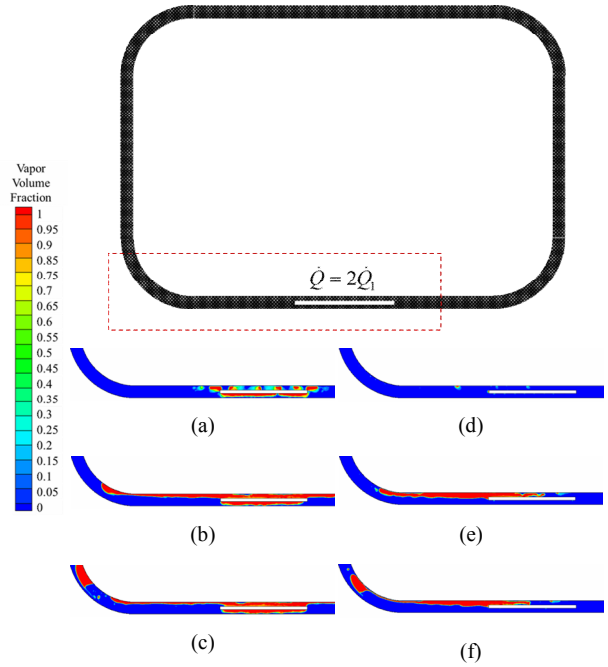

Fig. 8. Volume fraction distribution around a heater in case 02: (a) t = 1.2 s; (b) t = 4.1 s; (c) t= 4.5 s; (d) t = 40.6 s; (e) t = 53.0 s; (f) t = 53.1 s.

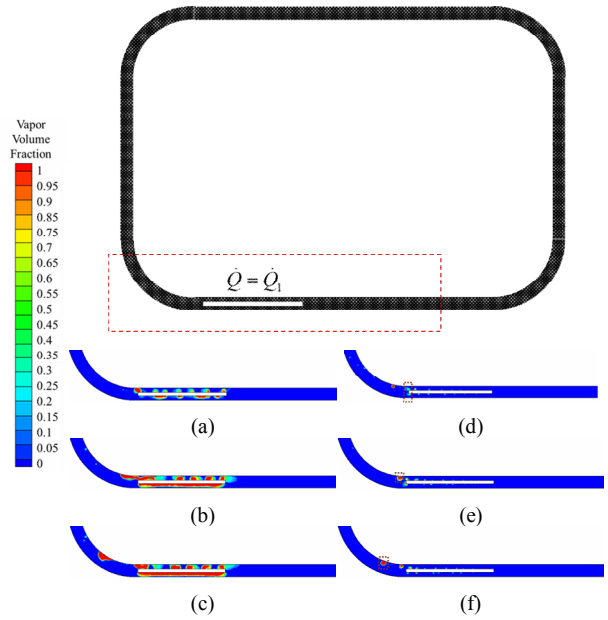

Fig. 9. Volume fraction distribution around a heater in case 03: (a) t = 1.2 s; (b) t = 2.3 s; (c) t = 2.4 s; (d) t = 32.7 s; (e) t = 33.4 s; (f) t = 33.55 s.

The bubbles were detached immediately after nucleation at the heater surface, as shown in Figs. 9(d)-(f), while the generated bubbles aggregated at the initial stage, as shown in Figs. 9(a)-(c).

Fig. 10 shows the volume fraction distribution around the heater in case 05 at different times. In this case, the bubbles detached from the heater and circulated in the loop thermosyphon in the initial stage. At 0.7 s, bubbles started to separate

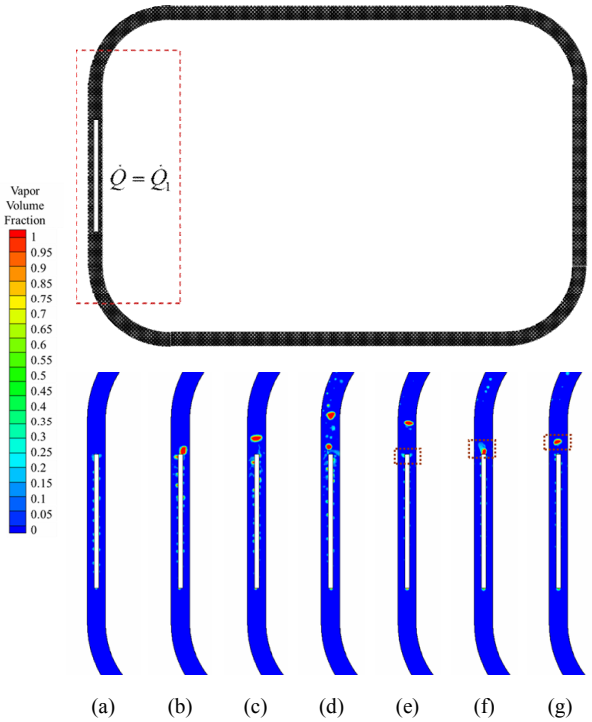

Fig. 10. Volume fraction distribution around a heater in case 05: (a) t = 0.35 s; (b) t = 0.55 s; (c) t = 0.7 s; (d) t = 1.2 s; (e) t = 33.4 s; (f) = 33.95 s; (g) t = 34.0 s.

from the heater, as shown in Fig. 10(c). The bubbles were continuously generated and detached from a heater. The size of bubbles was much smaller than that in the other cases. Therefore, the circulated bubbles in the loop thermosyphon easily condensed at the right side of the loop thermosyphon.

3.4 Average temperature

Fig. 11(a) shows a comparison of the average temperature for each case at 120 s. When a small amount of heat (Q1) was applied to the heater surface, the average temperature in case 03 was lowest among the three cases because the momentum of flow induced by bubbles generation was lowest among three tested geometries. The average temperature in case 05 was highest among the cases because the bubbles detached easily and heat was transferred well from heater to the liquid refrigerant in the BJLHP. However, the maximum difference in the average temperature among the cases was only about 1.6 °C. The average temperature increased when the heating power increased. When the heating power increased, the evaporation mass transfer rate increased because the temperature differences between the heater and working fluid increased. Fig. 11(b) shows a comparison of the RMS of the temperature for each case at 120 s. The RMS of the temperature was lowest in case 03 and highest in case 05 when a small amount of heat (Q_1) was applied to the heater surface. The order of the RMS of temperature among the three geometries was the same when a large amount of heat (Q_2) was applied to

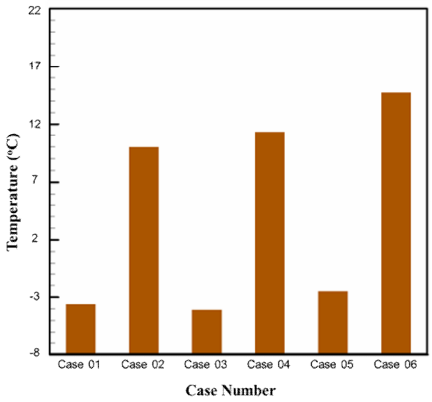

(a)

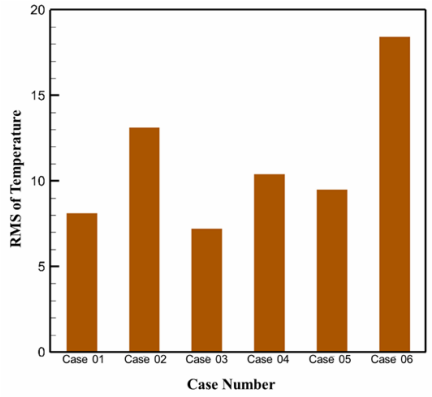

(b)

Fig. 11. Comparison of (a) average temperature; (b) RMS of temperature for each case at t = 120 s.

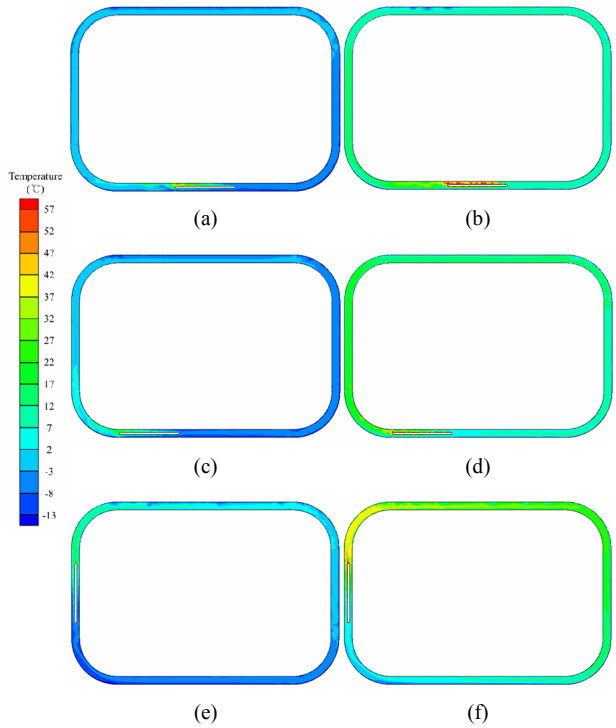

Fig. 12. Temperature distribution for each case at t = 120 s: (a) Case 1; (b) case 2; (c) case 3; (d) case 4; (e) case 5; (f) case 6.

the heater surface. The difference in the RMS of temperature among the three geometries increased when a large amount of heat (Q_2) was applied to the heater surface.

Fig. 12 shows the temperature distribution for each case at 120 s. When a large amount of heat (Q_2) was applied to the heater surface, the temperature increased and was widely distributed in all geometries, as shown in Figs. 13(b), (d) and (f). When the heater was located horizontally on the bottom left of the loop thermosyphon, the pressure in the loop thermosyphon was lowest among the three geometries, as shown in Fig. 5. Therefore, the RMS of temperature was lowest among the three geometries because the bubbles moved through the loop thermosyphon easily, as shown in Figs. 12(c) and (d).

When the heater was located vertically on the left center of the loop thermosyphon, the bubbles detached easily, and the average temperature was highest among the three cases. However, the high temperature region was narrowly distributed at the top left curved pipe, as shown in Figs. 12(e) and (f). In cases 05 and 06, the bubbles moved from the heater to the top side of the loop thermosyphon, while in cases 03 and 04, the bubbles moved to the left side. The bubbles moved slowly in cases 05 and 06 because the bubbles that detached from the heater moved through the horizontal pipe in cases 05 and 06, while bubbles also moved faster in the upward direction through the vertical pipe in other geometries due to the buoyancy force.

4. Conclusions

A numerical study on the two-phase flow pattern and temperature distribution in a loop thermosyphon was carried out with different locations of the heater and different values of heating power. The simulation was solved for 2D geometries using ANSYS FLUENT 15.0. To consider evaporation and condensation in the loop thermosyphon, the VOF method was applied to describe the interface between the vapor and liquid using UDFs. To simulate the compression of the vapor in the thermosyphon, the ideal gas law was applied to the R-134a vapor. The thermophysical properties of R-134a except for the gas density were varied as a function of temperature.

To study the effects of the heater location and heating power, three different models were designed, and two heating power conditions were considered. The heater was inserted inside the loop thermosyphon, and convective boundary conditions were applied to the outside wall of the loop thermosyphon. When the heating power increased, bubbles were generated frequently. Thus, the average temperature and RMS of temperature increased, and the temperature distribution was non-uniform.

The thermal performance was evaluated by comparing the average temperature and temperature uniformity in the loop thermosyphon. The average temperature was highest when the

heater was located vertically on the left of the loop thermosyphon. The RMS of temperature was lowest when the heater was located horizontally on the bottom left of the loop thermosyphon. When the heater was located horizontally on the bottom center, the average pressure in the loop thermosyphon was highest. Therefore, in regard to temperature uniformity, it is better to locate the heater on the bottom left of the loop thermosyphon, while for the average temperature, it is better to locate the heater vertically on the left.

Acknowledgments

This work was supported by the National Research Foundation of Korea (NRF) grant funded by the Korea government (MSIT) (NRF-2017R1C1B2007296 and NRF-2017R1A2B 3004883).

Nomenclature

ρ	: Density
α	: Volume fraction
$\vec{v}$	: Velocity vector
μ	: Viscosity
S_M	: Mass source term
p	: Pressure
h	: Enthalpy
S_E	: Energy source term
G_k	: Generation of turbulence kinetic energy
G_ω	: Generation of ω
Γ_k	: Effective diffusivity of k
Γ_ω	: Effective diffusivity of ω
T_{sat}	: Saturation temperature
L	: Latent heat of evaporation

References

[1] B. Fadhl, L. C. Wrobel and H. Jouhara, Numerical modelling of the temperature distribution in a two-phase closed thermosiphon, *Applied Thermal Engineering,* 60 (2013) 122-131.

[2] B. Fadhl, L. C. Wrobel and H. Jouhara, CFD modelling of a two-phase closed thermosyphon charged with R134a and R404a, *Applied Thermal Engineering,* 78 (2015) 482-490.

[3] L. M. Poplaski, A. Faghri and T. L. Bergman, Analysis of internal and external thermal resistances of heat pipes including fins using a three-dimensional numerical simulation, *International Journal of Heat and Mass Transfer,* 102 (2016) 455-469.

[4] S. Lin, J. Broadbent and R. McGlen, Numerical study of heat pipe application in heat recovery systems, *Applied Thermal Engineering,* 25 (2005) 127-133.

[5] S. Touahri and T. Boufendi, Numerical study of the conjugate heat transfer in a horizontal pipe heated by joulean effect, *Thermal Science*, 16 (2012) 53-67.

[6] T. Daimaru, S. Yoshida and H. Nagai, Study on thermal cycle in oscillating heat pipes by numerical analysis, *Applied Thermal Engineering,* 113 (2017) 1219-1227.

[7] W. Qu and H. B. Ma, Theoretical analysis of startup of a pulsating heat pipe, *International Journal of Heat and Mass Transfer,* 50 (2007) 2309-2316.

[8] K. Kafeel and A. Turan, Simulation of the response of a thermosyphon under pulsed heat input conditions, *International Journal of Thermal Sciences,* 80 (2014) 33-40.

[9] L. Asmaie, M. Haghshenasfard, A. Mehrabani-Zeinabad and M. N. Esfahany, Thermal performance analysis of nanofluids in a thermosyphon heat pipe using CFD modeling, *Heat Mass Transfer,* 49 (2013) 667-678.

[10] W. Lian, W. Chang and Y. Xuan, Numerical investigation on flow and thermal features of a rotating heat pipe, *Applied Thermal Engineering,* 101 (2016) 92-100.

[11] R. Ranjan, J. Y. Murthy, S. V. Garimella and U. Vadakkan, A Numerical model for transport in flat heat pipes considering wick microstructure effects, *International Journal of Heat and Mass Transfer*, 54 (2011) 153-168.

[12] N. Minocha, J. B. Joshi, A. K. Nayak and P. K. Vijayan, 3D CFD simulation of passive decay heat removal system under boiling conditions: Role of bubble sliding motionon inclined heated tubes, *Chemical Engineering Science*, 145 (2016) 245-265.

[13] A. S. Annamalai and V. Ramalingam, Experimental investigation and computational fluid dynamics analysis of a air cooled condenser heat pipe, *Thermal Science*, 15 (2011) 759-772.

[14] S. C. K. D. Schepper, G. J. Heynderickx and G. B. Marin, Modeling the evaporation of a hydrocarbon feedstock in the convection section of a steam cracker, *Computers and Chemical Engineering,* 33 (2009) 122-132.

[15] A. Alizadehdakhel, M. Rahimi and A. A. Alsairafi, CFD modeling of flow and heat transfer in a thermosyphon, *International Communications in Heat and Mass Transfer,* 37 (2010) 312-318.

[16] Z. Lin, S. Wang, R. Shirakashi and L. W. Zhang, Simulation of a miniature oscillating heat pipe in bottom heating mode using CFD with unsteady modeling, *International Journal of Heat and Mass Transfer,* 57 (2013) 642-656.

[17] S. M. Pouryoussefi and Y. Zhang, Numerical investigation of chaotic flow in a 2D closed-loop pulsating heat pipe, *Applied Thermal Engineering,* 98 (2016) 617-627.

[18] W. Kalata, K. J. Brown and R. J. Schick, Injector study via VOF: Emphasis on vapor condensation due to spray, *23rd Annual Conference on Liquid Atomization and Spray Systems* (2011).

[19] W. Lei, L. Yanzhonga, L. Zhan and Z. Kanga, Numerical investigation of thermal distribution and pressurization behavior in helium pressurized cryogenic tank by introducing a multicomponent model, *25th International Cryogenic Conference & International Cryogenic Materials Conference* (2014).

[20] Y. U. Gu, D. K. Jeong, J. H. Hwang, Y. H. Kwon and J. S. Kim, Study on defrost of evaporator using bubble jet loop heat pipe as a defrost device, *10th International Heat Pipe Symposium* (2011).

[21] ANSYS FLUENT, *Theory Guide (Release 15.0). Multi-phase Flows*, ANSYS, Inc. (2013) 465-600 (chapter 17).
[22] Thermo-physical properties of fluid system, NIST webbook, *NIST database*, http://webbook.nist.gov/chemistry/fluid/.

Man-Yeong Ha received his B.S. degree from Pusan National University, Korea, in 1981, M.S. degree, in 1983, from Korea Advanced Institute of Science and Technology, Korea, and Ph.D. degree from Pennsylvania State University, USA in 1990. Dr. Ha is currently a Professor at the School of Mechanical Engineering at Pusan National University in Busan, Korea. He serves as an Editor of the Journal of Mechanical Science and Technology. His research interests are focused on thermal management, computational fluid dynamics, and micro/nano fluidics.

Yong Gap Park received his B.S. degree from Pusan National University, Korea, in 2008, and Ph.D. degree from Pusan National University, Korea in 2014. Dr. Park is currently a Research Professor at Rolls-Royce and Pusan National University Technology Centre in Thermal Management, in Busan, Korea. His research interests are focused on natural convection, heat exchanger and computational fluid dynamics.

Seong Hyun Park received her B.S. degree from Pusan National University, Korea, in 2010. He started attending Pusan National University for the integrated Ph.D. program under the supervision of professor Man Yeong Ha. His research interests are focused on numerical simulation on two phase flow with phase change and heat exchanger.